



ELSEVIER

Comput. Methods Appl. Mech. Engrg. 143 (1997) 175–194

---

**Computer methods  
in applied  
mechanics and  
engineering**

---

# Shape-memory alloys: modelling and numerical simulations of the finite-strain superelastic behavior

Ferdinando Auricchio<sup>a,\*</sup>, Robert L. Taylor<sup>b</sup>

<sup>a</sup>Università di Roma 'Tor Vergata', Dipartimento di Ingegneria Civile, Via della Ricerca Scientifica, 00133 Roma, Italy

<sup>b</sup>University of California at Berkeley, Berkeley, California, USA

Received 31 January 1996

---

## Abstract

*Shape-memory alloys* (SMA) show features not present in materials traditionally used in engineering; as a consequence, they are the basis for innovative applications. The present work proposes a step toward the development of a computation tool to be used during the design of SMA-based devices. To reach this goal, we develop a constitutive model which reproduce the superelastic behavior of shape-memory alloys at finite strains. For an isothermal case we discuss in detail the numerical implementation within a finite-element scheme as well as the form of the algorithmically consistent tangent. To assess the viability of the proposed approach we simulate the response of some simple SMA typical structures (uniaxial test, four-point bending test) as well as an application with possibly a very high impact in different medical fields.

---

## 1. Introduction

Solid materials are not necessarily characterized by a unique pre-defined microscopic configuration. As an example, *shape-memory alloys* can change their crystallographic structure depending on the temperature and the state of stress.

As a natural consequence of the crystallographic changes, at the macroscopic level the shape-memory materials present the superelastic effect (the recovery of large deformations in a loading–unloading cycles, occurring at sufficiently high temperatures) and the shape-memory effect (the recovery of large deformations by a combination of mechanical and thermal processes).<sup>1</sup>

Both the superelastic and the shape-memory effect are in general not present in traditional materials. Hence, shape-memory alloy lend themselves to be successfully adopted in a broad set of advanced applications. Striking examples of devices exploiting superelasticity are orthodontic wires [9] and self-expanding micro-structures used in the treatment of hollow-organ or duct-system occlusions [19]. Examples of applications exploiting the shape-memory effect are the SMA fasteners (ranging from airplane-pipe couplings to computer-board connectors) or devices for the deployment and the control of space structures (antennas and satellites).

Due to the increasing degree of sophistication in SMA-based devices, there is a growing need for computational tools able to support the design process.

Clearly, the first step toward the preparation of computational tools is the development of constitutive models able to reproduce the material macroscopic behavior for complex states of stress or

---

\* Corresponding author. E-mail: auricchio@tovvx1.ccd.utovrm.it

<sup>1</sup> In the following, the following abbreviations are used: SMA for shape-memory alloy, SE for superelastic effect or superelasticity, SME for shape-memory effect.

loading patterns. However, the formulation of a constitutive model for shape-memory alloys is by itself a difficult task, one of the major reason being that conventional inelastic theories do not provide an adequate framework.

Recently, a new inelastic theory based on the internal variable formalism has been proposed [14]. The theory, based on the definition of elastic range and on the use of set theory, is a flexible environment for the development of constitutive models for materials with complex behaviors. Within this framework, Auricchio et al. have proposed a small-deformation three-dimensional model for the superelastic behavior of shape-memory material [3].

Using the same framework and a description of the evolution processes similar to the one adopted for the small deformation regime, the present paper extends the superelastic constitutive model to the case of finite strains.

The goal of the work is to propose a further step toward the development of a computational tool able to help the design process of SMA devices. Accordingly, the emphasis of the paper is direct toward the assessment of the ability to perform analyses of real devices. For this reason, after a survey of shape-memory-alloy features, a three-dimensional model able to reproduce the superelastic behavior within a large strain regime is presented. An integration algorithm and the algorithmically consistent tangent are carefully addressed. Then, the simulation of typically SMA structures is presented and discussed; in particular, the response of a real device, currently investigated as a profitable industrial application, is analyzed.

## 2. Shape-memory alloys

### 2.1. General features

Shape-memory alloys can undergo reversible changes in the crystallographic symmetry-point-group. Such changes can be interpreted as martensitic phase transformations, that is, as solid–solid diffusion-less phase transformations between a crystallographically more-ordered phase, the *austenite* or *parent phase*, and a crystallographically less-ordered phase, the *martensite* [12,27]. Typically, the austenite is stable at high temperatures and high values of the stress. For a stress-free state we indicate with  $T_f^{SA}$  the temperature above which only the austenite is stable and with  $T_f^{AM}$  the temperature below which only the martensite is stable.

The phase transformations between austenite and martensite are the key to explain the superelasticity effect. For the simple case of uniaxial tensile stress a brief explanation follows (Fig. 1). Consider a specimen in the austenitic state and at a temperature greater than  $T_f^{SA}$ ; accordingly, at zero stress only the austenite is stable. If the specimen is loaded, while keeping the temperature constant, the material presents a nonlinear behavior (*ABC*) due to a stress-induced conversion of austenite into martensite. Upon unloading, while again keeping the temperature constant, a reverse transformation from martensite to austenite occurs (*CDA*) as a result of the instability of the martensite at zero stress. At the end of the loading–unloading process no permanent strains are present and the stress–strain path is a closed hysteresis loop.

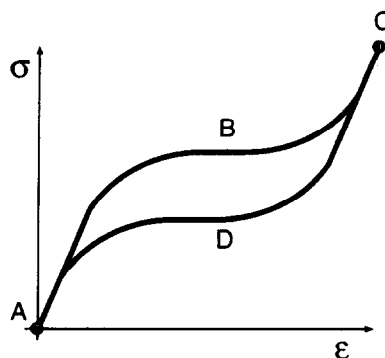


Fig. 1. Superelasticity.

At the crystallographic level, if there is no preferred direction for the occurrence of the transformation, the martensite takes advantage of the existence of different possible habit plates,<sup>2</sup> forming a series of crystallographically equivalent variants. The product phase is then termed *multiple-variant martensite* and is characterized by a *twinned* structure.

On the other hand, if there is a preferred direction for the occurrence of the transformation (often associated with a state of stress), all the martensite crystals tend to be formed on the most favorable habit plane. The product phase is then termed *single-variant martensite* and is characterized by a *detwinned* structure.

According to the existence of different types of single-variant martensitic species, the conversion of each single-variant martensite into different single variants is possible. Such process, known as *reorientation process*, can be interpreted as a family of martensitic phase transformations and is associated with changes in the parameters governing the single-variant martensite production (hence, it is often associated to nonproportional changes of stresses).

The martensitic transformations occurring in SMA are *thermoelastic* and *athermal* [25]. Thermoelastic means that the accommodation of the martensite plates within the parent phase is essentially elastic, with no dislocation generation; the interface remains glissile, capable of backward movements, and the reverse transformation proceeds through shrinkage of martensite plates. Athermal means that the amount of martensite formed is a function only of the temperature and not of the length of time at which the alloy is held at that temperature. Athermal transformations start at well-defined temperatures, which are usually insensitive to rate-effects.

## 2.2. Ni–Ti shape-memory material

Shape-memory properties for nickel (Ni) titanium (Ti) alloys were discovered in the 1960s, at the Naval Ordnance Laboratory (NOL) [6]; hence, the acronym NiTi–NOL or Nitinol, which is commonly used when referred to Ni–Ti based shape-memory alloys. Starting from the 1970s, Ni–Ti has been widely investigated due to its frequent use in applications [8,10,26] and today it is probably the shape-memory materials most frequently used in commercial applications.

A detailed discussion of crystallographic aspects, including possible self-accommodation mechanisms, can be found in [5,15,20,21].

The amount of heat recoverable memory strain and the size of the hysteresis loop strongly depend on alloy composition, thermomechanical processing, testing direction and deformation mode (that is, if the material is in simple tension, simple compression or shear) [1,18]. For the full austenite–martensite phase transformation the recoverable memory strain is of the order of 8%, while the hysteresis width is typically of 30–50°C.

For uniaxial states of stress and in the usual range of applications the stress-temperature regions in which the phase transformations may occur are delimited with good approximation by straight lines with slopes ranging from 2.5 MPa/°C to over 15 MPa/°C. Experimental evidence shows that:

- Phase transformations do not exhibit pressure dependence in the case of long-aged Ni–Ti; for short-aged Ni–Ti the R-phase (B2–R) transition is unaffected by pressure, while the martensitic (R–B19') transformation is pressure dependent [11].
- Phase transformations are insensitive to temperature rates and to stress rates [7].

## 3. A model for the SMA superelastic behavior

### 3.1. Control and internal variables

As control variables, we assume the Kirchhoff stress,  $\tau$ , and the temperature,  $T$ . To capture the effects induced by the phase transformations, we assume a multiplicative decomposition of the deformation gradient  $F$  in the form:

<sup>2</sup> By definition, the *habit plane* is the contact plane between the austenite and the martensite during a single-crystal transformation [12,27].

$$\mathbf{F} = \mathbf{F}^e \mathbf{F}^{tr} \quad (1)$$

where  $\mathbf{F}^e$  is the elastic part of the deformation gradient and  $\mathbf{F}^{tr}$  is an internal variable related to the phase transformations.<sup>3</sup>

Following Auricchio et al. [3], we do not distinguish between the different variants in which the martensite may be present; accordingly, we introduce a scalar parameter,  $\xi_s$ , representing the *single-variant martensite* fraction.

### 3.2. Phase transformations and activation conditions

We consider three phase transformations:

- the conversion of austenite into single-variant martensite ( $A \rightarrow S$ ),
- the conversion of single-variant martensite into austenite ( $S \rightarrow A$ ),
- the reorientation of the single-variant martensite ( $S \rightarrow S$ ).

We assume that there is no change in the martensitic fraction during the reorientation process, that is, the  $S \rightarrow S$  process occurs at constant value of the martensitic fraction. Accordingly, we assign a change of  $\xi_s$  only to the first two processes and write:<sup>4</sup>

$$\dot{\xi}_s = \dot{\xi}_s^{AS} + \dot{\xi}_s^{SA} \quad (2)$$

Each of the three phase transformations is assumed to occur in a specific region of the control-variable hyperplane  $\boldsymbol{\tau} - T$ , as discussed in the following.

#### 3.2.1. Conversion of austenite into single-variant martensite ( $A \rightarrow S$ )

To model the pressure dependence of phase transformations occurring in some alloys [11], we introduce a Drucker–Prager-type loading function:

$$F^{AS}(\boldsymbol{\tau}, T) = \|\mathbf{t}\| + 3\alpha p - C^{AS}T \quad (3)$$

where  $\mathbf{t}$  is the deviatoric part of the stress (defined as:  $\mathbf{t} = \boldsymbol{\tau} - \text{tr}(\boldsymbol{\tau})\mathbf{1}/3$ ),  $p$  is the pressure,  $C^{AS}$  and  $\alpha$  are material parameters and  $\|\cdot\|$  indicates the Euclidean norm. The initial and final transformation function can be expressed as:

$$F_s^{AS} = F^{AS} - R_s^{AS} \quad (4)$$

$$F_f^{AS} = F^{AS} - R_f^{AS} \quad (5)$$

with

$$R_s^{AS} = \left[ \sigma_s^{AS} \left( \sqrt{\frac{2}{3}} + \alpha \right) - C^{AS}T_s^{AS} \right] \quad (6)$$

$$R_f^{AS} = \left[ \sigma_f^{AS} \left( \sqrt{\frac{2}{3}} + \alpha \right) - C^{AS}T_f^{AS} \right] \quad (7)$$

where  $\sigma_s^{AS}$ ,  $\sigma_f^{AS}$ ,  $T_s^{AS}$  and  $T_f^{AS}$  are all material parameters. We assume that the conditions for the conversion of austenite into single-variant martensite are

$$F_s^{AS} > 0, \quad f_f^{AS} > 0, \quad \dot{F}^{AS} > 0 \quad (8)$$

For the evolution of the single-variant martensite fraction we may assume either an exponential form:

<sup>3</sup> The multiplicative split of the deformation gradient [13,17] is consistent with a large part of the literature on finite-deformation inelastic models. See [22] for a review and a discussion of the multiplicative split from a computational point of view.

<sup>4</sup> By convention, the superscripts refer to specific evolution processes; accordingly, the superscript  $AS$  refers to the conversion of austenite into single-variant martensite, while the superscript  $SA$  refers to the conversion of single-variant martensite into austenite.

$$\dot{\xi}_s^{AS} = H^{AS} \beta^{AS} (1 - \xi_s) \frac{\dot{F}^{AS}}{(F_f^{AS})^2} \quad (9)$$

with  $\beta^{AS}$  a material parameter, measuring the speed of the transformation, or a linear form:

$$\dot{\xi}_s^{AS} = -H^{AS} (1 - \xi_s) \frac{\dot{F}^{AS}}{F_f^{AS}} \quad (10)$$

The scalar parameter  $H^{AS}$  embeds the conditions for the activation of the phase transformation (Eq. (8)) and it is defined by the relation:

$$H^{AS} = \begin{cases} 1 & \text{if } F_s^{AS} > 0, \quad F_f^{AS} < 0, \quad \dot{F}^{AS} > 0 \\ 0 & \text{otherwise} \end{cases} \quad (11)$$

### 3.2.2. Conversion of single-variant martensite into austenite ( $S \rightarrow A$ )

Similarly to the above, we introduce a Drucker–Prager-type loading function:

$$F^{SA}(\tau, T) = \|\tau\| + 3\alpha p - C^{SA}T \quad (12)$$

where  $C^{SA}$  is a material parameter. The initial and final transformation functions can be expressed as

$$F_s^{SA} = F^{SA} - R_s^{SA} \quad (13)$$

$$F_f^{SA} = F^{SA} - R_f^{SA} \quad (14)$$

with

$$R_s^{SA} = \left[ \sigma_s^{SA} \left( \sqrt{\frac{2}{3}} + \alpha \right) - C^{SA} T_s^{SA} \right] \quad (15)$$

$$R_f^{SA} = \left[ \sigma_f^{SA} \left( \sqrt{\frac{2}{3}} + \alpha \right) - C^{SA} T_f^{SA} \right] \quad (16)$$

where  $\sigma_s^{SA}$ ,  $\sigma_f^{SA}$ ,  $T_s^{SA}$ ,  $T_f^{SA}$  are all material parameters. We assume that the conditions for the conversion of single-variant martensite into austenite are

$$F_s^{SA} < 0, \quad F_f^{SA} > 0, \quad \dot{F}^{SA} < 0 \quad (17)$$

For the evolution of the single-variant martensite fraction we may assume either an exponential form:

$$\dot{\xi}_s^{SA} = H^{SA} \beta^{SA} \xi_s \frac{\dot{F}^{SA}}{(F_f^{SA})^2} \quad (18)$$

with  $\beta^{SA}$  a material parameter, measuring the speed of the transformation, or a linear form:

$$\dot{\xi}_s^{SA} = H^{SA} \xi_s \frac{\dot{F}^{SA}}{F_f^{SA}} \quad (19)$$

The scalar parameter  $H^{SA}$  embeds the conditions for the phase transformation (Eq. (17)) and it is defined by the relation:

$$H^{SA} = \begin{cases} 1 & \text{if } F_s^{SA} < 0, \quad F_f^{SA} > 0, \quad \dot{F}^{SA} < 0 \\ 0 & \text{otherwise} \end{cases} \quad (20)$$

### 3.2.3. Single-variant martensite reorientation process ( $S \rightarrow S$ )

To model the single-variant martensite reorientation process for nonproportional changes of stress (changes of direction or rotation), we set

$$F^{SS} = \|\tau\| + 3\alpha p - C^{SS}T \quad (21)$$

$$\mathbf{F}_s^{SS} = \mathbf{F}^{SS} - \mathbf{R}_s^{SS} \quad (22)$$

with

$$\mathbf{R}_s^{SS} = \left[ \sigma_s^{SS} \left( \sqrt{\frac{2}{3}} + \alpha \right) - C^{SS} T_s^{SS} \right] \quad (23)$$

where  $C^{SS}$ ,  $\sigma_s^{SS}$  and  $T_s^{SS}$  are material parameters. We assume that the condition for the activation of the reorientation process is

$$f_s^{SS} > 0 \quad (24)$$

**REMARK 3.1.** From a physical point of view it seems plausible that whenever the material has enough energy to induce a conversion of single-variant martensite into austenite, then it has also enough energy to reorient the martensite fraction already present. Hence, we set  $C^{SA} = C^{SS}$  and  $\mathbf{R}_s^{SA} = \mathbf{R}_s^{SS}$ , such that  $\mathbf{F}_s^{SA} = \mathbf{F}_s^{SS}$ . Accordingly, we may conclude that whenever  $\xi_s > 0$ , then the reorientation process is active.

### 3.3. Elastic constitutive equation

Assuming the elastic response to be isotropic, the free-energy function is an isotropic function; hence, it can be expressed in terms of the elastic left Cauchy–Green tensor  $\mathbf{b}^e = \mathbf{F}^e \mathbf{F}^{e,T}$ , that is

$$\psi = \psi(\mathbf{b}^e) \quad (25)$$

The Kirchhoff stress is then given by

$$\boldsymbol{\tau} = 2(\partial \mathbf{b}^e \psi) \mathbf{b}^e \quad (26)$$

Due to isotropy, the principal directions of the Kirchhoff stress  $\boldsymbol{\tau}$  and the elastic left Cauchy–Green tensor  $\mathbf{b}^e$  coincide; accordingly, the following spectral decomposition can be introduced:

$$\boldsymbol{\tau} = \sum_{A=1}^3 \tau_A \mathbf{n}^A \otimes \mathbf{n}^A \quad (27)$$

$$\mathbf{b}^e = \sum_{A=1}^3 (\lambda_A^e)^2 \mathbf{n}^A \otimes \mathbf{n}^A \quad (28)$$

and from Eq. (26) we get

$$\tau_A = 2 \frac{\partial \psi}{\partial (\lambda_A^e)^2} (\lambda_A^e)^2 \quad (29)$$

We assume a free-energy function which is uncoupled in a deviatoric and a volumetric part:

$$\psi = W(\bar{\lambda}_A^e) + U(J^e) \quad (30)$$

where  $J^e = \lambda_1^e \lambda_2^e \lambda_3^e$  is the elastic volume and  $\bar{\lambda}_A^e = (J^e)^{-1/3} \lambda_A^e$  are the deviatoric principal stretches. Both  $W$  and  $U$  are assumed quadratic in the principle elastic logarithmic stretches  $\log(\lambda_A^e)$ :

$$W(\bar{\lambda}_A^e) = G \sum_{A=1}^3 [\log(\bar{\lambda}_A^e)]^2 \quad (31)$$

$$U(J^e) = \frac{1}{2} K [\log(J^e)]^2 \quad (32)$$

Exploiting Eq. (29), we deduce that

$$\tau_A = K \log(J^e) + 2G \log(\bar{\lambda}_A^e) \quad (33)$$

Hence, the Kirchhoff stress can be written as the sum of a volumetric and a deviatoric contribution:

$$\boldsymbol{\tau} = p\mathbf{1} + \mathbf{t} \quad (34)$$

with

$$p = K \log(J^e) \quad (35)$$

and

$$\mathbf{t} = \sum_{A=1}^3 t_A \mathbf{n}^A \otimes \mathbf{n}^A \quad (36)$$

$$t_A = 2G \log(\bar{\lambda}_A^e) \quad (37)$$

Finally, we assume an additive strain decomposition:

$$\mathbf{e}_A = \mathbf{e}_A^e + \epsilon_L \xi_S \mathbf{n}_A \quad (38)$$

$$\boldsymbol{\theta} = \boldsymbol{\theta}^e + 3\alpha \epsilon_L \xi_S \quad (39)$$

expressed in terms of the principal logarithmic stretches, where  $\epsilon_L$  is a scalar parameter representing the maximum deformation obtainable only by detwinning of the multiple-variant martensite. Accordingly, we have

$$e_A = \log(\bar{\lambda}_A) \quad \theta = \log(J) \quad (40)$$

$$e_A^e = \log(\bar{\lambda}_A^e) \quad \theta^e = \log(J^e) \quad (41)$$

where  $J = \lambda_1 \lambda_2 \lambda_3$  and  $\mathbf{n}_A = \mathbf{t}_A / \|\mathbf{t}\|$  with  $\|\mathbf{t}\| = [\sum_{A=1}^3 (t_A)^2]^{1/2}$ . Starting from Eqs. (38)–(39), exploiting the logarithmic expressions and taking the exponential of both sides, we get

$$\bar{\lambda}_A = \bar{\lambda}_A^e \exp(\epsilon_L \xi_S \mathbf{n}_A) \quad (42)$$

$$J = J^e \exp(3\alpha \epsilon_L \xi_S) \quad (43)$$

which are consistent with the multiplicative decomposition of the deformation gradient introduced in Eq. (1).

### 3.4. Material-parameter specialization to uniaxial states

The model presented so far is in a three-dimensional context. Accordingly, the material parameters involved in the constitutive equations are relative to a three-dimensional setting.

If the model is specialized to the case of uniaxial states of stress and strain, then the constitutive equations should involve the corresponding one-dimensional quantities, which are indicated herein with a superposed tilde and which may be easily computed from the corresponding three-dimensional parameters through the relations

$$\beta^{AS} = \tilde{\beta}^{AS} \left( \sqrt{\frac{2}{3}} + \alpha \right) \quad (44)$$

$$\beta^{SA} = \tilde{\beta}^{SA} \left( \sqrt{\frac{2}{3}} + \alpha \right) \quad (45)$$

$$\epsilon_L = \tilde{\epsilon}_l / \left( \sqrt{\frac{2}{3}} + \alpha \right) \quad (46)$$

## 4. Time-discrete isothermal models and algorithmic implementations

This section describes a time-discrete isothermal version of the three-dimensional model previously presented. The algorithmic implementation of the model within a finite-element framework and the form of the consistent tangent tensor are discussed.

While during the development of the time-continuous model we assumed stress and temperature as control variables, during the development of the isothermal time-discrete models we assume the strain as the only control variable. This choice is consistent with the fact that, from the point of view of integration scheme, the time-discrete problem is considered strain-driven. Accordingly, we consider two time values, say  $t_n$  and  $t_{n+1} > t_n$ , such that  $t_{n+1}$  is the first time value of interest after  $t_n$ . Then, knowing the strain at time  $t_{n+1}$  and the solution at time  $t_n$ , we should compute the new solution at time  $t_{n+1}$ . To minimize the appearance of subscripts (and to make the equations more readable), we introduce the convention

$$\mathbf{a}_n = \mathbf{a}(t_n), \quad \mathbf{a} = \mathbf{a}(t_{n+1})$$

where  $\mathbf{a}$  is any generic quantity. Therefore, the subscript  $n$  indicates a quantity evaluated at time  $t_n$ , while no subscript indicates a quantity evaluated at time  $t_{n+1}$ .

#### 4.1. Time-discrete model

Using a backward-Euler integration formula, the discrete form of Eq. (2) is

$$\xi_S = \xi_{S,n} + (\lambda_S^{AS} + \lambda_S^{SA}) \quad (47)$$

where

$$\lambda_S^{AS} = \int_{t_n}^{t_{n+1}} \dot{\xi}_S^{AS} dt \quad (48)$$

$$\lambda_S^{SA} = \int_{t_n}^{t_{n+1}} \dot{\xi}_S^{SA} dt \quad (49)$$

Similarly, using a backward-Euler scheme to integrate the time-continuous evolutionary equations yields the corresponding time-discrete evolutionary equations. Written in residual form and clearing fractions, the time-discrete evolutionary equations specialize to

$$\mathcal{R}^{AS} = (F_f^{AS})^2 \lambda_S^{AS} - H^{AS} \beta^{AS} (1 - \xi_S) (F^{AS} - F_n^{AS}) = 0 \quad (50)$$

$$\mathcal{R}^{SA} = (F_f^{SA})^2 \lambda_S^{SA} - H^{SA} \beta^{SA} \xi_S (F^{SA} - F_n^{SA}) = 0 \quad (51)$$

for the exponential case (Eqs. (9) and (18)), while for the linear case (Eqs. (10) and (19)) they specialize to:

$$\mathcal{R}^{AS} = F_f^{AS} \lambda_S^{AS} + H^{AS} (1 - \xi_S) (F^{AS} - F_n^{AS}) = 0 \quad (52)$$

$$\mathcal{R}^{SA} = F_f^{SA} \lambda_S^{SA} - H^{SA} \xi_S (F^{SA} - F_n^{SA}) = 0 \quad (53)$$

The quantities  $\lambda_S^{AS}$  and  $\lambda_S^{SA}$  can be computed expressing  $F^{AS}$  and  $F^{SA}$  as functions of  $\lambda_S^{AS}$  and  $\lambda_S^{SA}$  and requiring the satisfaction of  $\mathcal{R}^{AS}$  and  $\mathcal{R}^{SA}$ .

#### 4.2. Integration algorithm

A return-map algorithm is used as integration scheme for the time-discrete model. Initially suggested for the solution of plasticity formulations [16,29], the return map provides an efficient and robust integration scheme based on a discrete enforcement of the evolutionary equations [22,24]. It belongs to the family of elastic-predictor/inelastic-corrector algorithms and, hence, is a two-part algorithm. In the first part, a purely elastic *trial state* is computed; in the second part, if the trial state violates the constitutive model, an *inelastic correction* is computed using the trial state as an initial condition.

Following [2,22,23], as a consequence of the isotropy assumption, the return map algorithm developed within the framework of the infinitesimal theory carries over to the finite deformation context with minor modifications.



Adopting an updated-Lagrangian formulation [4], we introduce the relative deformation gradient  $\mathbf{f}$ :

$$\mathbf{f} = \mathbf{I} + \frac{\partial \mathbf{u}}{\partial \mathbf{x}_n} \quad (54)$$

and split the deformation gradient and the deformation Jacobian:

$$\mathbf{F} = \mathbf{f} \mathbf{F}_n \quad (55)$$

$$J = \det(\mathbf{f}) J_n \quad (56)$$

The details of the algorithm are as follows:

(1) *Compute elastic trial left Cauchy–Green tensor.* Assume that no phase transformations occur (i.e.  $\xi_s = \xi_{s,n}$ ,  $\lambda_s^{AS} = \lambda_s^{SA} = 0$ ). Accordingly, compute the elastic trial left Cauchy–Green tensor:

$$\mathbf{b}^{e,TR} = \mathbf{f} \mathbf{b}_n^e \mathbf{f}^T$$

(2) *Compute spectral decomposition of  $\mathbf{b}^{e,TR}$ .* Compute  $\mathbf{n}^{A,TR} = \mathbf{n}^A$  and  $(\lambda_A^{e,TR})^2$ .

(3) *Compute trial Kirchhoff stress.*

$$\boldsymbol{\tau}^{TR} = p^{TR} \mathbf{1} + \mathbf{t}^{TR}$$

where

$$\mathbf{t}^{TR} = \sum_{A=1}^3 t_A^{TR} \mathbf{n}^A \otimes \mathbf{n}^A$$

$$p^{TR} = K \log(J^{e,TR})$$

$$t_A^{TR} = 2G \log[(J^{e,TR})^{-1/3} \lambda_A^{e,TR}]$$

(4) *Check phase transformations.* Check if the conditions for the occurrence of the phase transformations are satisfied.

(5) *Return map.* If some of the phase-transformation conditions are satisfied, the parameters  $\lambda_s^{AS}$  and  $\lambda_s^{SA}$  are computed requiring the satisfaction of the time-discrete evolutionary equations.

(6) *Compute algorithmic tangent.*

**REMARK 4.1.** Step 5 is performed solving Eqs. (50)–(51) or Eqs. (52)–(53) using a Newton-type iterative algorithm:

$$\begin{Bmatrix} (\lambda_s^{AS})^{k+1} \\ (\lambda_s^{SA})^{k+1} \end{Bmatrix} = \begin{Bmatrix} (\lambda_s^{AS})^k \\ (\lambda_s^{SA})^k \end{Bmatrix} - \mathbf{R}^{-1} \begin{Bmatrix} (R^{AS})^k \\ (R^{SA})^k \end{Bmatrix} \quad (57)$$

where

$$\mathbf{R}^{-1} = \begin{bmatrix} \frac{\partial R^{AS}}{\partial \lambda_s^{AS}} & \frac{\partial R^{AS}}{\partial \lambda_s^{SA}} \\ \frac{\partial R^{SA}}{\partial \lambda_s^{AS}} & \frac{\partial R^{SA}}{\partial \lambda_s^{SA}} \end{bmatrix}^{-1} = \begin{bmatrix} a & b \\ c & d \end{bmatrix}^{-1} = \begin{bmatrix} B & C \\ D & E \end{bmatrix} \quad (58)$$

and the superscript  $k$  indicates the iteration index. The checks for detecting the occurrence of the phase transformations are described in [3].

#### 4.3. Algorithmic tangent

In the following we address the construction of the tangent matrix consistent with the time-discrete model. The use of a consistent tangent tensor preserves the quadratic convergence of the Newton

method, which we adopt for the incremental solution of the momentum equations from a finite-element scheme.

Following [2,22,23], the linearization of the material part of the Kirchhoff stress leads to a symmetric matrix with a functional form similar to the algorithmic tangent of the infinitesimal theory.

Linearizing the elastic constitutive relations and Eq. (47), we get

$$dp = K[d\theta - 3\alpha\epsilon_L(d\lambda_s^{AS} + \lambda_s^{SA})] \quad (59)$$

$$dt = 2G\{de - \epsilon_L[(d\lambda_s^{AS} + d\lambda_s^{SA})n + \xi_s dn]\} \quad (60)$$

where

$$n = \frac{t}{\|t\|} = \frac{e}{\|e\|} \quad (61)$$

As proved in [3], we have

$$dn = d\left(\frac{t}{\|t\|}\right) = d\left(\frac{e}{\|e\|}\right) = \frac{1}{\|e\|} [I - n \otimes n] de \quad (62)$$

where

$$\|e\| = \|t\|/(2G) + \epsilon_L \xi_s \quad (63)$$

and  $I$  is the second-order identity tensor. Accordingly:

$$dp = K d\theta - 3K\alpha\epsilon_L(d\lambda_s^{AS} + d\lambda_s^{SA}) \quad (64)$$

$$dt = 2G \left[ I - \epsilon_L \xi_s \frac{1}{\|e\|} (I - n \otimes n) \right] de - 2G\epsilon_L(d\lambda_s^{AS} + d\lambda_s^{SA})n \quad (65)$$

The scalar quantities  $d\lambda_s^{AS}$  and  $d\lambda_s^{SA}$  are computed from the linearization of the discrete-time evolutionary equations (Eqs. (50)–(51) for the exponential model and Eqs. (52)–(53) for the linear model) as function of  $\epsilon$ ,  $\lambda_s^{AS}$  and  $\lambda_s^{SA}$ :

$$d\lambda_s^{AS} = (T_1^{AS}n + T_2^{AS}\mathbf{1}) : d\epsilon \quad (66)$$

$$d\lambda_s^{SA} = (T_1^{SA}n + T_2^{SA}\mathbf{1}) : d\epsilon \quad (67)$$

where

$$T_1^{AS} = 2G(BA^{AS} + CA^{SA}) \quad (68)$$

$$T_2^{AS} = 3k\alpha(BA^{AS} + CA^{SA}) \quad (69)$$

$$T_1^{SA} = 2G(DA^{AS} + EA^{SA}) \quad (70)$$

$$T_2^{SA} = 3k\alpha(DA^{AS} + EA^{SA}) \quad (71)$$

and

$$A^{AS} = -\frac{\partial R^{AS}}{\partial F^{AS}} \quad (72)$$

$$A^{SA} = -\frac{\partial R^{SA}}{\partial F^{SA}} \quad (73)$$

Finally, we obtain

$$d\tau = D d\epsilon \quad (74)$$

where

$$D = [K^*(\mathbf{1} \otimes \mathbf{1}) + 2G^*I_{\text{dev}} + M_1^*(\mathbf{n} \otimes \mathbf{n}) - M_2^*(\mathbf{n} \otimes \mathbf{1} + \mathbf{1} \otimes \mathbf{n})] \quad (75)$$

with

$$K^* = K\{1 - 3\epsilon_L \alpha(T_2^{AS} + T_2^{SA})\} \quad (76)$$

$$2G^* = 2G \left\{ 1 - \epsilon_L \xi_s \frac{1}{\|\mathbf{e}\|} \right\} \quad (77)$$

$$M_1^* = 2G\epsilon_L \left[ \xi_s \frac{1}{\|\mathbf{e}\|} - (T_1^{AS} + T_1^{SA}) \right] \quad (78)$$

$$M_2^* = 2G\epsilon_L (T_2^{AS} + T_2^{SA}) \quad (79)$$

#### 4.4. Specialization to linear and exponential flow rules

We now consider how some of the quantities previously introduced specialize for the case of linear and exponential flow rules. First of all, we note that

$$\frac{\partial F^{AS}}{\partial \lambda_s^{AS}} = \frac{\partial F^{AS}}{\partial \lambda_s^{SA}} = [2G + 9K\alpha^2]\epsilon_L = G_1 \quad (80)$$

$$\frac{\partial F^{SA}}{\partial \lambda_s^{AS}} = \frac{\partial F^{SA}}{\partial \lambda_s^{SA}} = [2G + 9K\alpha^2]\epsilon_L = G_1 \quad (81)$$

Accordingly, for the *linear* flow rule, we have

$$a = -G_1 \lambda_s^{AS} - [(F^{AS} - F_n^{AS}) + (1 - \xi_s)G_1] + F_f^{AS} \quad (82)$$

$$b = -G_1 \lambda_s^{AS} - [(F^{AS} - F_n^{AS}) + (1 - \xi_s)G_1] \quad (83)$$

$$c = -G_1 \lambda_s^{SA} - [(F^{SA} - F_n^{SA}) - \xi_s G_1] \quad (84)$$

$$d = -G_1 \lambda_s^{SA} - [(F^{SA} - F_n^{SA}) - \xi_s G_1] + F_f^{SA} \quad (85)$$

and

$$A^{AS} = -\frac{\partial \mathcal{R}^{AS}}{\partial F^{AS}} = -\lambda_s^{AS} - (1 - \xi_s) \quad (86)$$

$$A^{SA} = -\frac{\partial \mathcal{R}^{AS}}{\partial F^{AS}} = -\lambda_s^{SA} + \xi_s \quad (87)$$

For the *exponential* flow rule, we have

$$a = \beta^{AS}(F^{AS} - F_n^{AS}) + G_1[\beta^{AS}(1 - \xi_s) - 2\lambda_s^{AS}F_f^{AS}] + (F_f^{AS})^2 \quad (88)$$

$$b = \beta^{AS}(F^{AS} - F_n^{AS}) + G_1[\beta^{AS}(1 - \xi_s) - 2\lambda_s^{AS}F_f^{AS}] \quad (89)$$

$$c = -\beta^{SA}(F^{SA} - F_n^{SA}) + G_1[\beta^{SA}\xi_s - 2\lambda_s^{SA}F_f^{SA}] \quad (90)$$

$$d = -\beta^{SA}(F^{SA} - F_n^{SA}) + G_1[\beta^{SA}\xi_s - 2\lambda_s^{SA}F_f^{SA}] + (F_f^{SA})^2 \quad (91)$$

and

$$A^{AS} = -\frac{\partial \mathcal{R}^{AS}}{\partial F^{AS}} = -2\lambda_s^{AS}F_f^{AS} + \beta^{AS}(1 - \xi_s) \quad (92)$$

$$A^S - A = -\frac{\partial \mathcal{R}^{AS}}{\partial F^{AS}} = -2\lambda_s^{SA}F_f^{SA} + \beta^{SA}\xi_s \quad (93)$$

## 5. Finite-element simulation of shape-memory-alloy devices

We now want to assess our ability to perform simulations for typical SMA-based devices exploiting the superelastic behavior.

The material adopted is a standard binary Ni–Ti alloy [3,28]. The experimental data as well as the specimen specifications were provided by Dr. A.R. Pelton and Dr. T.W. Duerig of Nitinol Device & Components, Inc.<sup>5</sup>

### 5.1. Material-parameter characterization

The first step is to properly identify the parameters to use in the material constitutive model.

As discussed in [3], we consider the results from two uniaxial tension tests performed on a circular wire of diameter  $D = 1.49$  mm, controlling the displacements (Figs. 2 and 3). From the inspection of the experimental stress-strain curves the following material parameters are chosen for both the exponential and the linear model:

$$E = 60000 \text{ MPa}, \quad \nu = 0.3, \quad \tilde{\epsilon}_L = 7.5\%$$

$$T_s^{AS} = T_f^{AS} = 0^\circ\text{C}, \quad C^{AS} = 0 \text{ MPa}/^\circ\text{C}$$

$$T_s^{SA} = T_f^{SA} = 0^\circ\text{C}, \quad C^{SA} = 0 \text{ MPa}/^\circ\text{C}$$

For the exponential model we also set

$$\sigma_s^{AS} = 520 \text{ MPa}, \quad \sigma_f^{AS} = 750 \text{ MPa}, \quad \tilde{\beta}^{AS} = 250 \text{ MPa}$$

$$\sigma_s^{SA} = 550 \text{ MPa}, \quad \sigma_f^{SA} = 200 \text{ MPa}, \quad \tilde{\beta}^{SA} = 20 \text{ MPa}$$

while for the linear model we set

$$\sigma_s^{AS} = 520 \text{ MPa}, \quad \sigma_f^{AS} = 600 \text{ MPa}$$

$$\sigma_s^{SA} = 300 \text{ MPa}, \quad \sigma_f^{SA} = 200 \text{ MPa}$$

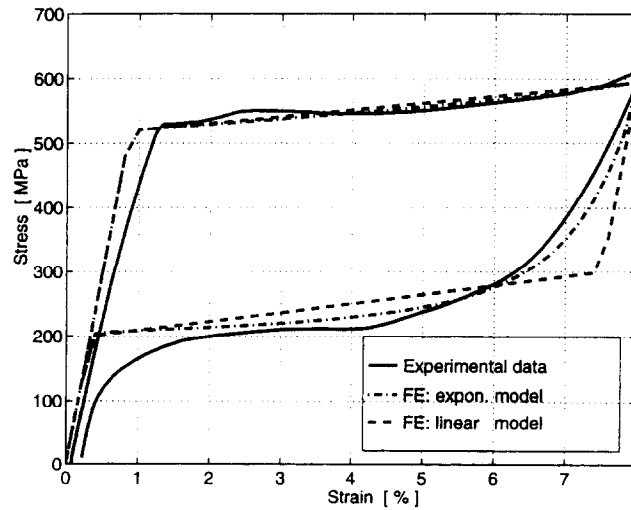


Fig. 2. Material-parameter characterization.

<sup>5</sup> Nitinol Device & Components, Inc., 48501 Warm Spring Blvd., Fremont, 94539 CA, USA.

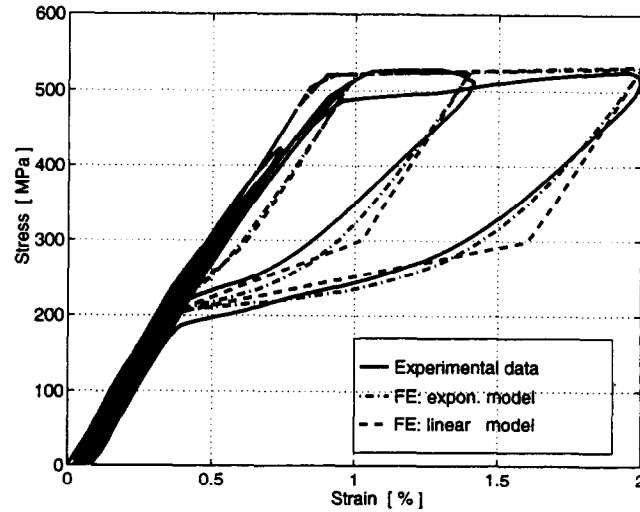


Fig. 3. Material-parameter characterization.

The stress–strain responses simulated using the exponential and the linear models are reported respectively with dash–dot and dash–dash lines in Figs. 2 and 3.

Due to the limited number of tension tests available, it is not possible to accurately assess the maximum deformation obtainable by detwinning of the multiple-variant martensite ( $\tilde{\epsilon}_L$ ), the starting and final values of the reverse transformation as well as the difference between the elastic properties of the austenite and the martensite. Accordingly, the values chosen for the parameters are quite arbitrary [3].

Finally, from consideration relative to a Ni–Ti–10% Cu alloy [14] the parameter  $\alpha$  is set equal to 0.15.

### 5.2. Four-point bending test

A four-point bending test was performed on a wire of circular cross section with diameter  $D = 1.49$  mm. The test procedure is described in [28].

The setting of the test is idealized in Fig. 4. The beam is simply supported on rollers, sitting at a fixed distance  $L = 20$  mm. The output parameters recorded during the experiments are the load  $F$  and the bottom fiber deflection of the beam middle-span section.

Due to symmetry conditions only half of the half-span beam needs to be studied. For the numerical simulations we use the mesh presented in Fig. 5. In Fig. 6 the plotted load–deflection curves are computed using the exponential model for the large-deformation regime. We report also the solution computed using the exponential model for the small-deformation model presented in [3].

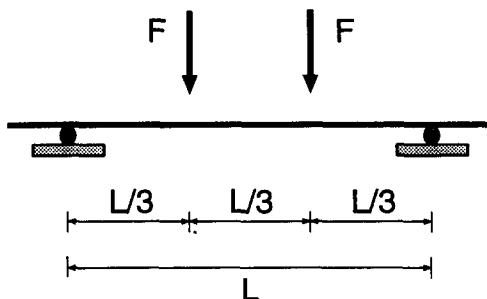


Fig. 4. Four-point bending test: test problem.



Fig. 5. Four-point bending test: finite-element mesh.

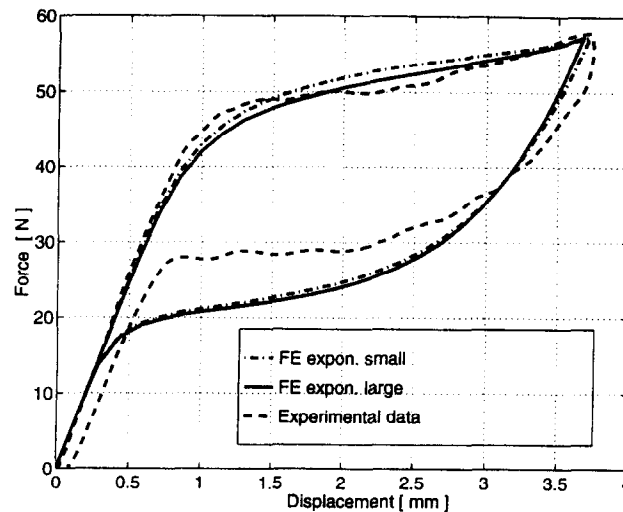


Fig. 6. Four-point bending test: finite element solution.

In Fig. 7 the plotted load–deflection curves are computed using both the exponential and the linear model for the large-deformation regime. The experimental load–deflection curve is also reported. From the inspection of the figures it is possible to conclude that:

- For the four-point bending test, the large-deformation analysis and the small-deformation analysis give comparable results.
- The predicted load–deflection curves match quite well the experimental data. However, the part of the curve corresponding to the final unloading portion and the size of the hysteresis loop differ from those found experimentally.
- The exponential and the linear models predict similar results, except in the part of the curve corresponding to the initial unloading portion.

### 5.3. Analysis of a stent

Stent is the technical word indicating self-expanding micro-structures, which are currently investigated for the treatment of hollow-organ or duct-system occlusions.

An example of a stent with a diamond pattern is given in Fig. 8. This structural typology can be

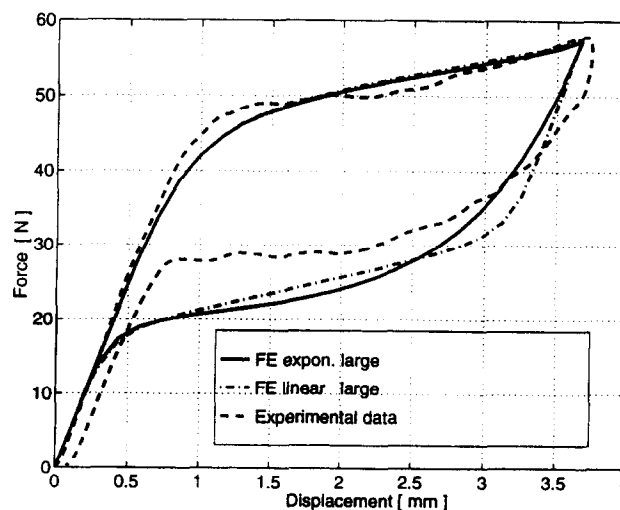


Fig. 7. Four-point bending test: finite element solution.

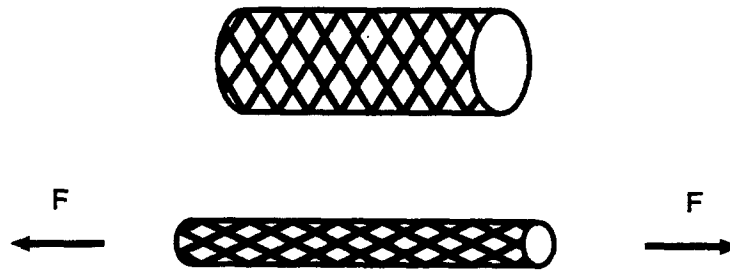


Fig. 8. Stent: a self-expanding micro-structure.

obtained from a SMA tube using a laser to cut out the diamond patterns. The diamond pattern geometry allows one to easily stretch the stent, which can then be safely and traumatically inserted due to its small profile. After being released from the delivery system, the stent self-expands to its original diameter and exerts a constant, gentle radial force on the vessel wall. The radius of the stretched-out stent can be as small as half of the original unstretched radius [19].

A diamond pattern spanning an angle  $\gamma$  is presented in Fig. 9. Due to the symmetry conditions only one quarter of a diamond pattern need to be modeled. The boundary conditions are set to respect all the restrictions imposed by the symmetries and still allow radial displacements (Fig. 10).

In the following we focus on a stent with  $\gamma = 40^\circ$ ,  $R_{\text{ext}} = 2.25$  mm,  $R_{\text{int}} = 2.00$  mm; other geometric dimensions are indicated in millimeters in Fig. 11. These values are estimated from a photograph and may differ from the ones used in actual design. The finite-element mesh is presented in Fig. 12. As output parameters we consider the axial load  $F$  and the displacement of node A, either in the axial direction or in the inward radial direction (Fig. 10).

We again use the material parameters estimated through the experimental uniaxial tests presented in Section 5.1.

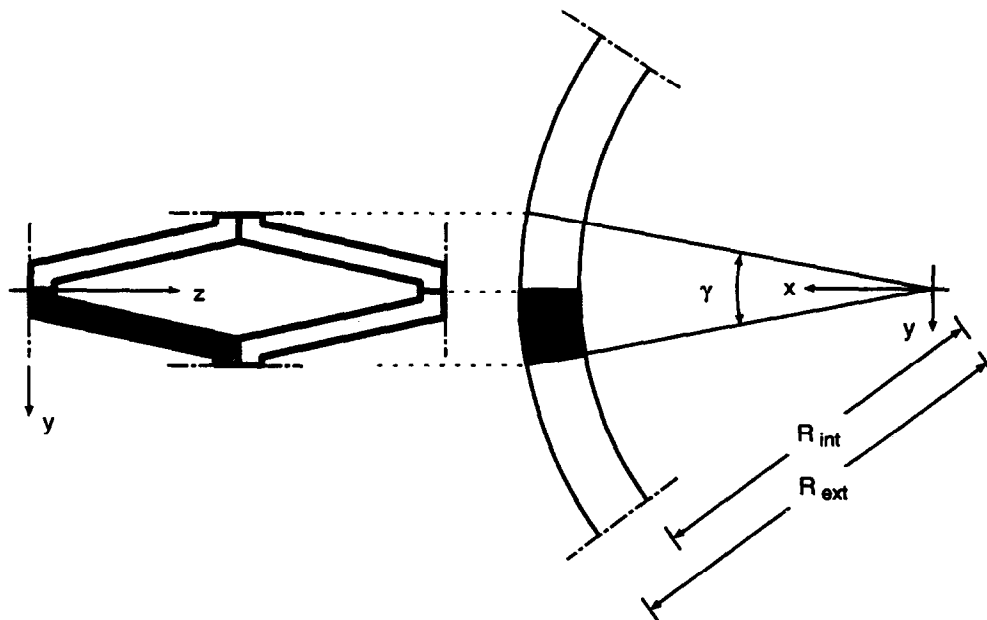


Fig. 9. Stent: diamond pattern.

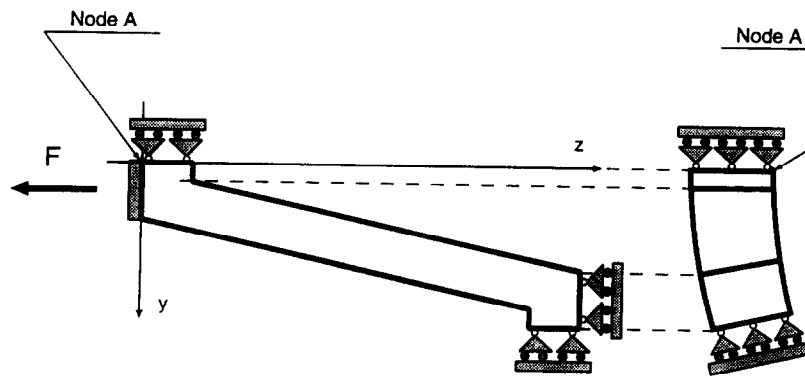


Fig. 10. Stent: model.

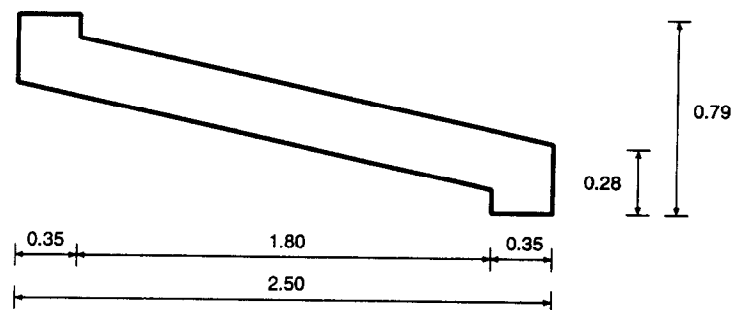


Fig. 11. Stent: plant.

We start by considering a load–unload history with a peak load of 20 N. In Figs. 13 and 14 we plot, respectively, the axial load versus the axial displacement and the axial load versus the radial displacement computed using the linear model for the small- and the large-deformation regimes. From an inspection of the figures it is possible to conclude that:

- For both the small- and the large-deformation regimes the radial displacement is one order larger than the axial displacement.
- The large-deformation analyses give very different results than the small-deformation analyses. In particular, during the large-deformation analyses a progressive stiffening of the structure due to geometric effects can be observed. Accordingly, for the particular structure under investigation (and differently from what previously observed for the four- and the three-point bending tests) the geometric effects are nonnegligible.

The same analyses were performed using the exponential model; the exponential and the linear models give very similar results in terms of global response parameters.

We also run a load–unload history bring the peak load up to 50 N. Due to the previous considerations, only the case of linear material model within a large-deformation regime is considered. In Figs. 15 and 16 we plot, respectively, the axial load versus the axial displacement and the axial load versus the radial displacement. It is very interesting to observe the unexpected radial displacement pattern, which indicates that, due to the particular geometry under investigation, the stent is unable to undergo radial displacements larger than 0.9 mm (i.e., less than 50% of the initial radius). Thus, from a practical point of view, the stent investigated is not optimal. This highlights the need for a better design



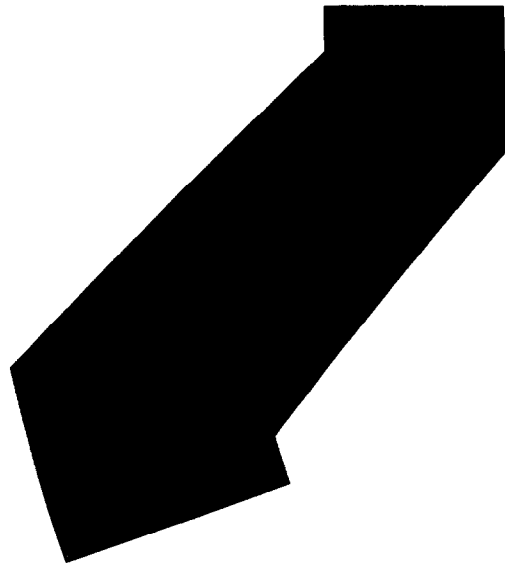


Fig. 12. Stent: finite-element mesh.

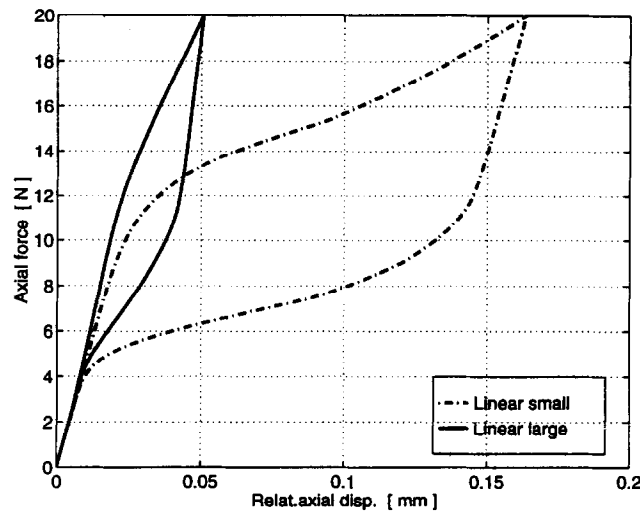


Fig. 13. Stent: finite-element solution.

for the particular geometry considered here, as well as the value of the proposed method in assessing proposed configurations.

## 6. Closure and future research directions

The present work proposes a further step toward the development of a computation tool to be used during the design of SMA-based devices. To reach this goal, we develop a constitutive model which reproduce some basic features of shape-memory alloys at finite strains, such as superelasticity, different material behavior in tension and compression, and the single-variant-martensite reorientation process.

For an isothermal case we discuss in detail the numerical implementation with a finite-element scheme as well as the form of the algorithmically consistent tangent.

To assess the viability of the proposed approach we simulate the response of some simple SMA

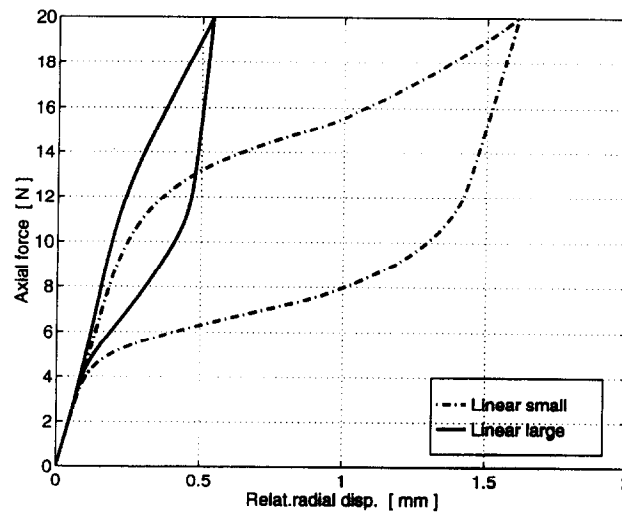


Fig. 14. Stent: finite-element solution.

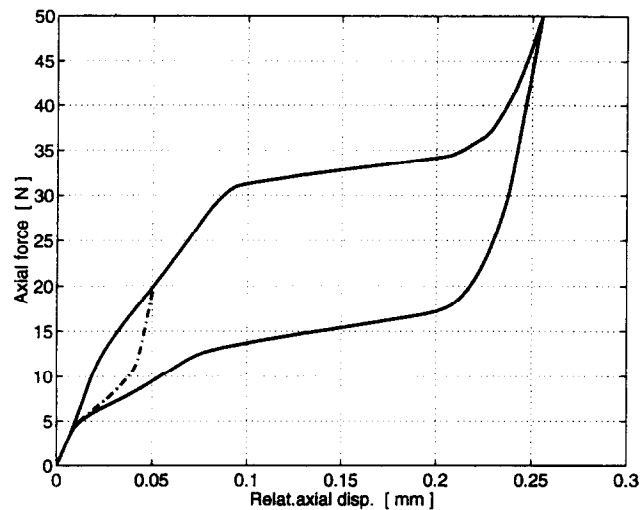


Fig. 15. Stent: finite-element solution.

typical structures (uniaxial test, four-point bending test) for which experimental data are available. From the simulations it is possible to evince that the proposed framework produces results which are in good agreement with the experimental data, especially considering that the material parameters used have been extrapolated on the basis of only two tension tests.

To validate the previous points, we also simulate the behavior of a SMA stent, which today is an application with possibly very high impact in different medical fields. For the particular geometry considered we are able to investigate the structural response and to find some limiting conditions in terms of maximum reduction of the stent diameter. These limiting conditions can be extremely valuable during a design process.

The overall discussion leads us to conclude that the proposed approach is a plausible initial development of an effective computational tool for the simulation of SMA-based devices. However, additional research and developments are needed in order to obtain a fully general and reliable tool. From the modeling point of view the required extensions and improvements are:

- implementation of a thermomechanical model able to simulate also the shape-memory effect
- more accurate assessment and modeling of the reorientation process for the single-variant martensites

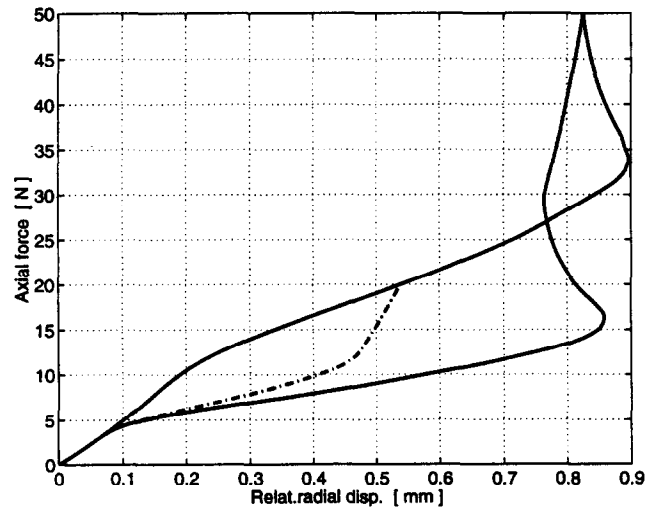


Fig. 16. Stent: finite-element solution.

- modeling of the different elastic properties of the austenite and the martensite.

All the proposed developments have to be followed by an experimental campaign, in order to better understand the material macroscopic behavior as well as the possible interaction between the different phase transformations.

## References

- [1] P.H. Adler, W. Yu, A.R. Pelton, R. Zadno, T.W. Duerig and R. Barresi, On the tensile and torsional properties of pseudoelastic Ni-Ti, *Scripta Metall. Mater.* 24 (1990) 943–947.
- [2] F. Armero and J.C. Simo, A priori stability estimates and unconditionally stable product formula algorithms for nonlinear coupled thermoplasticity, *Int. J. Plastic.* 9 (1993) 749–782.
- [3] F. Auricchio, R.L. Taylor and J. Lubliner, Shape-memory alloys: macromodelling and numerical simulations of the superelastic behavior (1996) submitted for publication.
- [4] K.J. Bathe, *Finite Element Procedures in Engineering Analysis* (Prentice-Hall, Englewood Cliffs, NJ, 1982).
- [5] W. Bührer, M. Zolliker and R. Gotthardt, Crystal structures of the shape memory alloy Ni-Ti (comments on recent publication in *Acta Metall. Mater.*), *Scripta Metall. Mater.* 26 (1992) 1149–1151.
- [6] W.J. Buehler and R.C. Wiley, Nickel-based alloys. Technical report, 1965, US-Patent 3174851.
- [7] A. Chrysochoos, M. Lobel and O. Maisonneuve, Thermomechanical coupling of pseudoelastic behaviour of CuZnAl and NiTi alloys, *CR Acad. Sci., Ser. II* 320 (1995) 217–223.
- [8] W.B. Cross, A.H. Kariotis and F.J. Stimler, Technical report, 1969. NASA SP 1433.
- [9] T.W. Duerig, K.N. Melton, D. Stökel and C.M. Wayman, eds. *Engineering Aspects of Shape Memory Alloys* (Butterworth-Heinemann, 1990).
- [10] C.M. Jackson, H.J. Wagner and R.J. Wasilewski, 55-Nitinol-the alloy with a memory: its physical metallurgy, properties and applications, Technical report, 1972. NASA SP 5110.
- [11] T. Kakeshita, K. Shimizu, S. Nakamichi, R. Tanaka, S. Endo and F. Ono, Effect of hydrostatic pressures on thermoelastic martensitic transformations in aged Ti-Ni and ausaged Fe-Ni-Co-Ti shape memory alloys, *Mater. Trans. JIM* (1992) 33: 1–6.
- [12] A.G. Khachaturyan, *Theory of Structural Transformations in Solids* (John Wiley & Sons, 1983).
- [13] E.H. Lee, Elastic-plastic deformation at finite strains, *J. Appl. Mech.* 36 (1969) 1–6.
- [14] J. Lubliner and F. Auricchio, Generalized plasticity and shape memory alloys, *Int. J. Solids Struct.* (1995), in press.
- [15] K. Madangopal, J. Singh and S. Banerjee, The nature of self accommodation in Ni-Ti shape memory alloys, *Scripta Metall. Mater.* 29 (1993) 725–728.
- [16] G. Maenchen and S. Sack, The tensor code, in: B. Alder, ed., *Methods in Computational Physics*, Vol. 3 (Academic Press, 1964) 181.
- [17] J. Mandel, Thermodynamics and plasticity, in: J.J. Delgado Dominguez, M.N.R. Nina and J.H., Whitelaw, eds., *Foundation of Continuum Thermodynamics* (1974) 283–304.
- [18] K.N. Melton, Ni-Ti based shape memory alloys, in: T.W. Duerig, K.N. Melton, D. Stökel and C.M. Wayman, eds., *Engineering Aspects of Shape Memory Alloys* (1990) 21–35.

- [19] A. Melzer and D. Stökel, Performance improvement of surgical instrumentation through the use of Ni–Ti materials, in: A.R. Pelton, D. Hodgson and T. Duerig, eds., *Proc. First International Conference on Shape Memory and Superelastic Technologies* (1994) 401–409.
- [20] S. Miyazaki, K. Otsuka and C.M. Wayman, The shape memory mechanism associated with the martensitic transformation in Ti–Ni alloys—I. Self-accommodation, *Acta Metall.* 37 (1989) 1873–1884.
- [21] S. Miyazaki, K. Otsuka and C.M. Wayman, The shape memory mechanism associated with the martensitic transformation in Ti–Ni alloys—II. Variant coalescence and shape recovery, *Acta Metall.* 37 (1989) 1885–1890.
- [22] J.C. Simo, Topics on the numerical analysis and simulation of plasticity, in: P.G. Ciarlet and J.L. Lions, eds., *Handbook of Numerical Analysis*, Vol. III (Elsevier Science Publisher B.V., 1996), in press.
- [23] J.C. Simo, Algorithms for static and dynamic multiplicative plasticity that preserve the classical return mapping schemes of the infinitesimal theory, *Comput. Methods Appl. Mech. Engrg.* 99 (1992) 61–112.
- [24] J.C. Simo and T.J.R. Hughes, *Elasto-plasticity and Visco-plasticity: Computational Aspects* (Springer-Verlag, 1996) in press.
- [25] I. Tamura and C.M. Wayman, Martensitic transformations and mechanical effects, in: G.B. Olson and W.S. Owen, eds., *Martensite: A Tribute to Morris Cohen* (1992) 227–242.
- [26] F.E. Wang, Proceeding of symposium of NiTi and related compounds. Technical report, 1968. NOLTR 68-16.
- [27] C.M. Wayman, *Introduction to the Crystallography of Martensitic Transformations* (MacMillan, 1964).
- [28] A. Wick, The bending behavior of superelastic NiTi. Master's thesis (Universität Karlsruhe (TH), Institut für Werkstoffkunde I, 1994).
- [29] M.L. Wilkins, Calculation of elastic plastic flow, in: B. Alder, ed., *Methods in Computational Physics*, Vol. 3 (Academic Press, 1964) 211.